Spin Echo Versus Stimulated Echo Diffusion Tensor Imaging of the In Vivo Human Heart

Constantin von Deuster,[1,2] Christian T. Stoeck,[1,2] Martin Genet,[2] David Atkinson,[3] and Sebastian Kozerke[1,2]*

Purpose: To compare signal-to-noise ratio (SNR) efficiency and diffusion tensor metrics of cardiac diffusion tensor mapping using acceleration-compensated spin-echo (SE) and stimulated echo acquisition mode (STEAM) imaging.
Methods: Diffusion weighted SE and STEAM sequences were implemented on a clinical 1.5 Tesla MR system. The SNR efficiency of SE and STEAM was measured (b = 50–450 s/mm^2) in isotropic agar, anisotropic diffusion phantoms and the in vivo human heart. Diffusion tensor analysis was performed on mean diffusivity, fractional anisotropy, helix and transverse angles.
Results: In the isotropic phantom, the ratio of SNR efficiency for SE versus STEAM, $SNR_t(SE/STEAM)$, was 2.84 ± 0.08 for all tested b-values. In the anisotropic diffusion phantom the ratio decreased from 2.75 ± 0.05 to 2.20 ± 0.13 with increasing b-value, similar to the in vivo decrease from 2.91 ± 0.43 to 2.30 ± 0.30. Diffusion tensor analysis revealed reduced deviation of helix angles from a linear transmural model and reduced transverse angle standard deviation for SE compared with STEAM. Mean diffusivity and fractional anisotropy were measured to be statistically different ($P < 0.001$) between SE and STEAM.
Conclusion: Cardiac DTI using motion-compensated SE yields a 2.3–2.9× increase in SNR efficiency relative to STEAM and improved accuracy of tensor metrics. The SE method hence presents an attractive alternative to STEAM based approaches. **Magn Reson Med 76:862–872, 2016. © 2015 The Authors. Magnetic Resonance in Medicine published by Wiley Periodicals, Inc. on behalf of International Society for Magnetic Resonance in Medicine. This is an open access article under the terms of the Creative Commons Attribution License, which permits use, distribution and reproduction in any medium, provided the original work is properly cited.**

Key words: myocardial fiber architecture; cardiac diffusion tensor imaging; STEAM; spin-echo, motion compensation; signal-to-noise ratio

[1]Imaging Sciences and Biomedical Engineering, King's College London, London, United Kingdom.

[2]Institute for Biomedical Engineering, University and ETH Zurich, Zurich, Switzerland.

[3]Centre for Medical Imaging, University College London, London, United Kingdom

*Correspondence to: Sebastian Kozerke, Ph.D., Institute for Biomedical Engineering University and ETH Zurich, Gloriastrasse 35, 8092 Zurich. E-mail: kozerke@biomed.ee.ethz.ch

INTRODUCTION

The fiber architecture of the heart has significant influence on cardiac function, mechanical contraction and electrophysiology (1–5). The principal orientation of myofibers can be obtained from histological studies (6–8) or ex vivo (9–11) and in vivo (12–24) diffusion tensor imaging (DTI). While histological exams provide localized information on myocyte orientation with very high spatial resolution ex vivo, cardiac DTI allows assessment of myofiber aggregates noninvasively and in vivo. In agreement with histology, ex vivo DTI studies have demonstrated the characteristic circumferential alignment of myofibers with a distinct double helical pattern from endo- to epicardium (25–27). Fiber disarray and myocardial remodeling due to myocardial infarction and cardiomyopathies have been assessed by DTI methods both in animal and humans subjects (28–33). Moreover, microstructural integrity of the myocardium has been described using mean diffusivity (MD) and fractional anisotropy (FA). Whereas mean diffusivity increased in myocardial infarction, FA was found to decrease (22,28,30,34). These findings highlight the potential of in vivo cardiac DTI to allow for structural and functional tissue characterization in a range of relevant diseases.

In vivo cardiac DTI has primarily been performed using the stimulated echo acquisition mode (STEAM) (12,13,15,17,18,20–23,33). Alternatively, spin-echo (SE) imaging is feasible provided that motion compensated diffusion gradients are employed or dedicated postprocessing to account for motion-induced signal loss is used (16,24,35–38). Image formation is typically accomplished using echo planar imaging (EPI) or balanced steady-state free precession imaging (39). Despite the advances in sequence design and data processing, DTI of the beating heart remains a challenging task due to low signal-to-noise-ratio (SNR), off-resonance artifacts, cardiac bulk motion, and myocardial strain.

In STEAM, diffusion encoding ranges across two consecutive heartbeats and hence the spatial position and shape of the myocardium are required to be identical in subsequent cardiac cycles. Accordingly, dedicated breath-holding and navigator gating schemes are essential to suppress respiratory motion induced displacements. Alternatively, free-
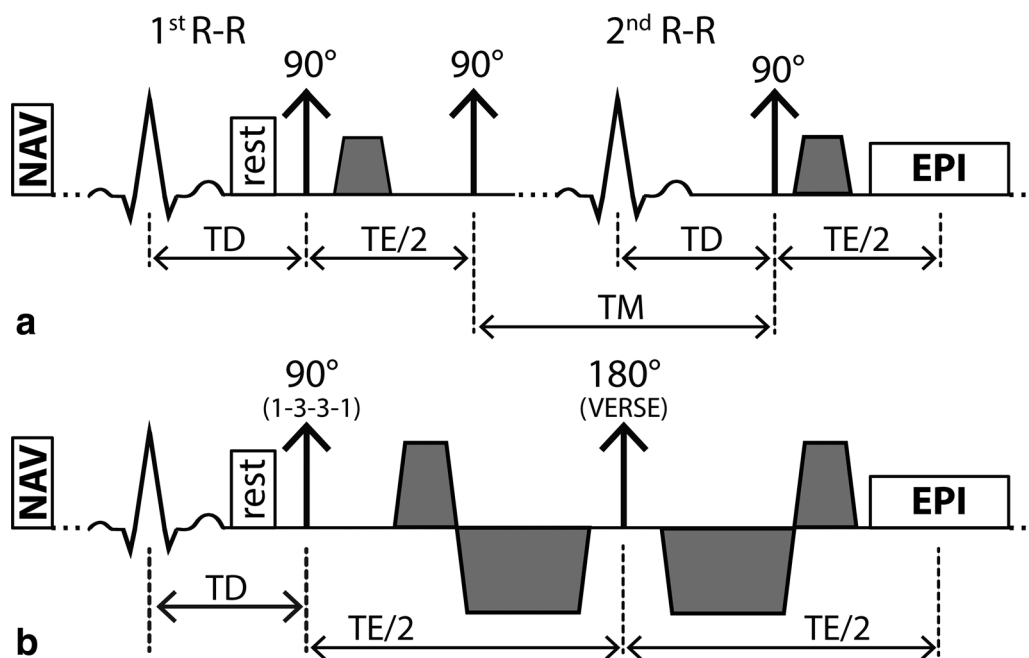
FIG. 1. Sequence diagrams. STEAM acquisition spanning over two consecutive heartbeats (**a**) and SE acquisition with second order motion compensated diffusion encoding gradients including VERSE (variable rate selective excitation) echo pulse (**b**). Fat suppression is achieved by a binomial excitation pulse. The excitation slab is tilted with respect to the 90° or 180° pulses to allow for reduced field of view imaging. Before the first 90° excitation, rest slabs are applied orthogonal to the field of view in phase encoding direction to suppress residually excited signal. For both sequences, the trigger delay was set to mid systole and images were encoded by identical single-shot EPI readouts.

breathing acquisition can be performed in combination with a dedicated navigator gating strategy and optional patient feedback system (18). The effect of myocardial strain during diffusion encoding using STEAM has to be considered by acquiring at so-called "sweet spots" (15) in the cardiac cycle. Alternatively, separately acquired strain data (20,23) may be used to correct for strain effects in the DTI data. A key advantage of STEAM over SE relates to the modest gradient hardware requirements as diffusion encoding takes place over a whole cardiac cycle and hence relatively low diffusion encoding gradient strengths are sufficient for adequate diffusion weighting.

With recent improvements in gradient hardware becoming widely available on clinical MR systems and dedicated diffusion gradient designs, diffusion weighted single-shot spin-echo (SE) sequences have become feasible for in vivo cardiac DTI. Several studies have shown that signal attenuation due to myocardial motion can be addressed successfully by incorporating motion compensated diffusion gradient waveforms (17,19,35–38,40–43). Promising results of the in vivo human (38) and rat (42) heart using second and third order motion compensated DTI have been presented recently.

While image and data quality depend on many parameters including residual motion, off-resonance and eddy-current effects (44), the low SNR of cardiac DTI is a significant impediment to wider adoption of the technique in the clinic. Besides the need for patient feedback (18) and dedicated data postprocessing (23,45), low scan time efficiency is a major reason for the small number of cardiac DTI studies on patients (46–48). Accordingly, a comparison of the available sequence approaches with regard to SNR and time efficiency is warranted to guide further improvements.

It is the objective of the present work to assess and compare SNR efficiency and diffusion metrics derived from cardiac DTI using acceleration-compensated diffusion-weighted SE and cardiac triggered STEAM in both phantoms and in the in vivo human heart.

METHODS

Figure 1 illustrates the ECG-triggered and diffusion weighted STEAM and SE sequences used in the present study. For the SE variant, second-order motion compensated diffusion gradients are used (38).

The SNR of SE and STEAM depend on sequence timing parameters (echo time: TE, repetition time TR, mixing time TM), tissue properties (relaxation times T1, T2, diffusivity D), imaging parameters (voxel size ΔV, number of signal averages NSA, flip angle α), and diffusion encoding strength b. Here SNR efficiency (i.e., SNR per unit time) for the SE and STEAM sequences is defined as:

$$SNR_t(SE) \propto \frac{1 - e^{-TR/T1}}{1 - \cos\alpha e^{-TR/T1}} \sin\alpha\, e^{-TE_{SE}/T2} e^{-b \cdot D} \frac{\Delta V}{\sqrt{NSA}} \quad [1]$$

$$SNR_t(STEAM)$$
$$\propto \frac{1}{2} \frac{1 - e^{-TR/T1}}{1 - \cos\alpha e^{-TR/T1}} \sin\alpha\, e^{-TM/T1} e^{-TE_{STEAM}/T2} e^{-b \cdot D} \frac{\Delta V}{\sqrt{NSA}\sqrt{2}} \quad [2]$$

In Eq. [2], the factors $1/2$ and $1/\sqrt{2}$ account for the inherent signal loss in STEAM and the fact that two cardiac cycles are required to encode the stimulated echo.
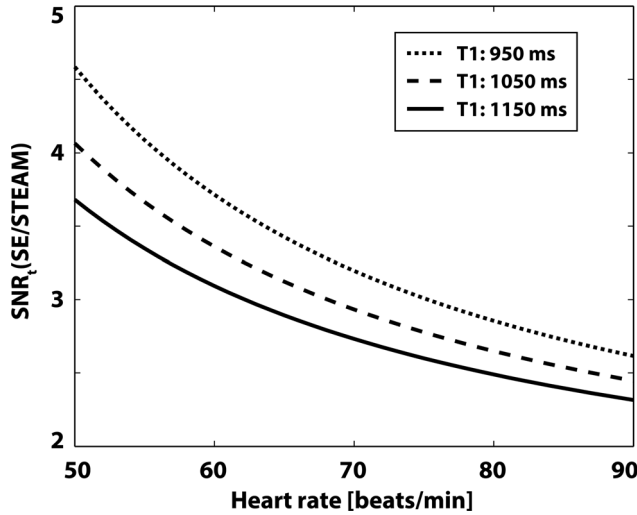
FIG. 2. Theoretical SNR efficiency. The SNR efficiency ratio of SE versus STEAM is seen to decrease with increasing heart rate. At a heart rate of 60 min^{-1}, b-value = 450 s/mm^2, TR/TE = 1000 ms/ 70 ms (SE), TR/TM/TE = 1000 ms/985/31 ms (STEAM) the relative gain in SNR efficiency of SE versus STEAM is 3.5$\times$.

Because of ECG triggering, TR and TM are determined by the subject's heart rate (HR) according to:

$$TR = \frac{60\,\text{min}^{-1}}{HR[\text{min}^{-1}]} \times 1000\,[\text{ms}] \quad TM = TR - \frac{TE_{STEAM}}{2}. \quad [3]$$

In Figure 2, the ratio of SNR efficiency for SE versus STEAM, SNR$_t$(SE/STEAM), is presented with sequence parameters according to the gradient system used in this study (b-value = 450 s/mm^2, TE$_{SE}$ = 70 ms, TE$_{STEAM}$ = 31 ms). The SNR$_t$(SE/STEAM) ratio is seen to decrease with increasing heart rate but remains greater than 2.3 up to heart rates of 90 min^{-1}. At a heart rate of 60 min^{-1} and T$_1$/T$_2$ = 1030/52 ms (49,50), the theoretical SNR gain of SE relative to STEAM is approximately 3.5$\times$.

Study Protocol

Cardiac SE and STEAM diffusion weighted imaging were implemented on a 1.5 Tesla (T) Philips Achieva System (Philips Healthcare, Best, The Netherlands) with gradients delivering 80 mT/m maximum strength at a slew rate of 100 mT/m/ms per physical axis. Signal was received with a five-channel cardiac receiver array. Written informed consent was obtained from all subjects before imaging. The study protocol was approved by the ethics committee of the Canton of Zurich. Consent included imaging as well as publication of anonymized data.

Phantom Measurements

A phantom with isotropic diffusivity was made from an aqueous agar solution with a concentration of 40 g/L. T1 was reduced by addition of 2.5 $\times$ 10^{-6} mmol/L Gadolinium (Primovist, Bayer Schering, Germany) and relaxation times determined by a vendor preimplemented imaging sequence (51): T1$_{Agar}$ = 1153 $\pm$ 10 ms,

T2$_{Agar}$ = 49.6 $\pm$ 0.4 ms within a region of interest inside the phantom.

To probe differences of the diffusion process during SE and STEAM diffusion encoding, a dedicated diffusion phantom with fiber structures mimicking cardiac myofibers was used in a second set of phantom measurements. The phantom consists of two crossing fiber bundles ($\sim$20 mm diameter) of hydrophobic polyethylene cords as described previously (52).

The SNR efficiency of SE and STEAM was determined for several b-values (50, 100, 200, 300, and 450 s/mm^2). Diffusion weighted images were acquired with in-plane resolution: 2.8 $\times$ 2.8 mm^2, slice thickness: 16 mm (isotropic phantom)/12 mm (anisotropic phantom), field of view (FOV): 230 $\times$ 98 mm^2, TR/TE (SE): 1000 ms/70 ms, TR/TE (STEAM): 1000 ms/31 ms, flip angle (SE, STEAM): 90°, four signal averages and six diffusion encoding directions (Table 1). To measure noise, the scans were repeated without RF and gradient pulses keeping the receiver gain and bandwidth the same as for actual imaging. Sufficient time (>10 s) was allowed between image and noise acquisition to ensure complete signal decay. SNR was determined for each voxel by dividing the absolute signal value of the diffusion weighted images by the standard deviation of the real part of complex noise in a local mask of 9 by 9 pixels. SNR$_t$(SE/STEAM) of the anisotropic diffusion phantom was corrected for different T1/T2 values between both phantoms (T1$_{diffusion\ phantom}$ = 934 $\pm$ 42 ms, T2$_{diffusion\ phantom}$ = 104.2 $\pm$ 4 ms).

DTI was performed without the b = 0 s/mm^2 image. Instead, three low diffusion weighted images (b = 100 s/ mm^2) were acquired along orthogonal directions along with nine additional diffusion weighted images (b = 450 s/ mm^2) distributed on the edge of a cube to maximize gradient usage and hence gradient strength. The duration of diffusion encoding gradients for the different diffusion weightings was kept the same and differences in b-values were achieved by scaling the gradient strength. Imaging parameters were as follows: in-plane resolution: 2.8 $\times$ 2.8 mm^2, slice thickness: 12 mm, FOV: 230 $\times$ 98 mm^2, TR/TE (SE): 1000 ms/70 ms, TR/TE (STEAM): 1000 ms/31 ms, number of signal averages: 16. To examine the effect of the sequence upon MD and FA, rather than any effects due to intrinsic SNR dependence (53), the flip angle of the SE excitation pulse was reduced to 16° to match SNR of the corresponding STEAM sequence (flip angle STEAM: 90°). Hence, variations in MD and FA can be uniquely assigned to differences during the diffusion encoding process.

In Vivo Measurements

Data were acquired in seven healthy subjects without history of cardiac disease (five female, weight 64 $\pm$ 6 kg, age 28 $\pm$ 6 years, heart rate 64 $\pm$ 10 beats/min, min/max heart rates: 49/89 beats/min). Before diffusion imaging, cine data with a temporal resolution of 10 ms were acquired in two chamber and short axis view orientations. According to the cine images, systolic quiescent time points were determined on a per subject basis with a mean delay of 316 $\pm$ 19 ms.

Diffusion weighted imaging was performed during breath-holding in short-axis view orientation with a

Table 1
Imaging Parameters of SNR and DTI Phantom Experiments

	Resolution	b-values [s/mm^2]	Flip angle [deg]	No. of directions	NSA (per b-value/dir.)
SNR measurement (isotropic phantom)					
SE	$2.8 \times 2.8 \times 16$mm^3	50,100,200,300,450	90	6	4
STEAM	$2.8 \times 2.8 \times 16$mm^3	50,100,200,300,450	90	6	4
SNR measurement (anisotropic phantom)					
SE	$2.8 \times 2.8 \times 12$mm^3	50,100,200,300,450	90	6	4
STEAM	$2.8 \times 2.8 \times 12$mm^3	50,100,200,300,450	90	6	4
DTI measurement (anisotropic phantom)					
SE	$2.8 \times 2.8 \times 12$mm^3	100,450	16	12	16
STEAM	$2.8 \times 2.8 \times 12$mm^3	100,450	90	12	16

reduced field-of-view (FOV) technique (54). Consistent levels of breath-holds were ensured by the use of a respiratory navigator placed on the right hemi diaphragm with a gating window of 5 mm. To avoid aliasing from residual excitation along the phase encoding direction, saturation slabs orthogonal to the imaging plane were played out before the RF excitation pulse (see Figure 1). A 1-3-3-1 binomial spatial-spectral excitation pulse for fat suppression (55) was used in the SE case. The duration of the 180° refocusing pulse was minimized using variable rate selective excitation (VERSE) (56) (Fig. 1). Diffusion weighting was performed by unipolar gradients (STEAM) and second order motion compensated gradient waveforms (SE) as proposed in (38,42).

To minimize the effects of myocardial strain, the STEAM sequence was timed to the systolic strain "sweet spot" (15). The centers of mass of the STEAM and SE diffusion gradients within an R–R interval were aligned, resulting in a trigger delay for the SE sequence of 45% peak systolic contraction. In vivo SNR measurements were performed in each volunteer similar to the phantom experiments with a slice thickness of 16 mm to increase SNR. To guarantee identical b-values for the SE and STEAM sequences, the effective b-values during STEAM acquisitions were calculated based on the actual heart rates recorded during the in vivo experiments. Additionally, sufficient time to recover between the breath-holds was ensured to avoid significant heart rate variations during scanning. To avoid magnetization transients during imaging, the first average was used as dummy scan and discarded.

For DTI, total scan time of the in vivo experiments was matched between SE and STEAM. Accordingly, 8 signal averages per diffusion encoding direction were acquired with STEAM, while 16 averages were recorded with SE (Table 2). The imaging slice (slice thickness: 8 mm) was positioned at a mid-ventricular level. Data acquisition was split into multiple breath-holds by

acquiring all signal averages of a single diffusion encoding direction during a single breath-hold. Between the breath-holds, sufficient time for complete relaxation of magnetization was insured.

Additionally, DTI and SNR measurements were repeated during respiratory navigator-gated free-breathing acquisition with identical imaging and sequence parameters. Data collection was performed in a subgroup (n = 4, all female, weight 61 ± 10 kg, age 26 ± 2 years, heart rate 60 ± 8 beats/min, min/max heart rates: 44/71 beats/min) of the seven healthy volunteers in a separate imaging session. The methods and results are listed in the Appendix and Supporting Figure S1, which is available online.

Data Analysis

The mean SNR of the phantom and in vivo data was determined for all acquired b-values ranging from b = 50 s/mm^2 to 450 s/mm^2. SNR efficiency ratios of the SE sequence relative to the STEAM approach were calculated and compared with the theoretical values according to equations [1] and [2] taking the individual sequence timing (TR, TM, TE) into account. Relaxation times (T1 = 1030 ms/T2 = 52 ms) were taken from literature (49,50).

For diffusion tensor analysis, images were first registered to the mean image using affine image transformations [elastix toolbox (57)]. The in vivo SNR was determined using myocardial contours. To avoid partial voluming effects, voxels at the epi and endocardial borders were excluded from the statistics. The actual b-values due to heart rate variations were corrected for by adjusting b_{100} and b_{450} to the corresponding true values and the b-matrix modified for the proposed sampling scheme. The corresponding set of equations reads:

$$B^\dagger \vec{S} = \vec{D} \qquad [4]$$

with the modified b-matrix:

Table 2
Imaging Parameters of SNR and DTI In Vivo Experiments

	Resolution	b-values [s/mm^2]	Flip angle [deg]	No. of directions	NSA (per b-value/dir.)
SNR measurement (in-vivo)					
SE	$2.8 \times 2.8 \times 16$mm^3	50,100,200,300,450	90	6	4
STEAM	$2.8 \times 2.8 \times 16$mm^3	50,100,200,300,450	90	6	4
DTI measurement (in-vivo)					
SE	$2.8 \times 2.8 \times 8$mm^3	100,450	90	12	16
STEAM	$2.8 \times 2.8 \times 8$mm^3	100,450	90	12	8

b=100s/mm²   **b=450s/mm²**   **SNR efficiency**

Spin Echo

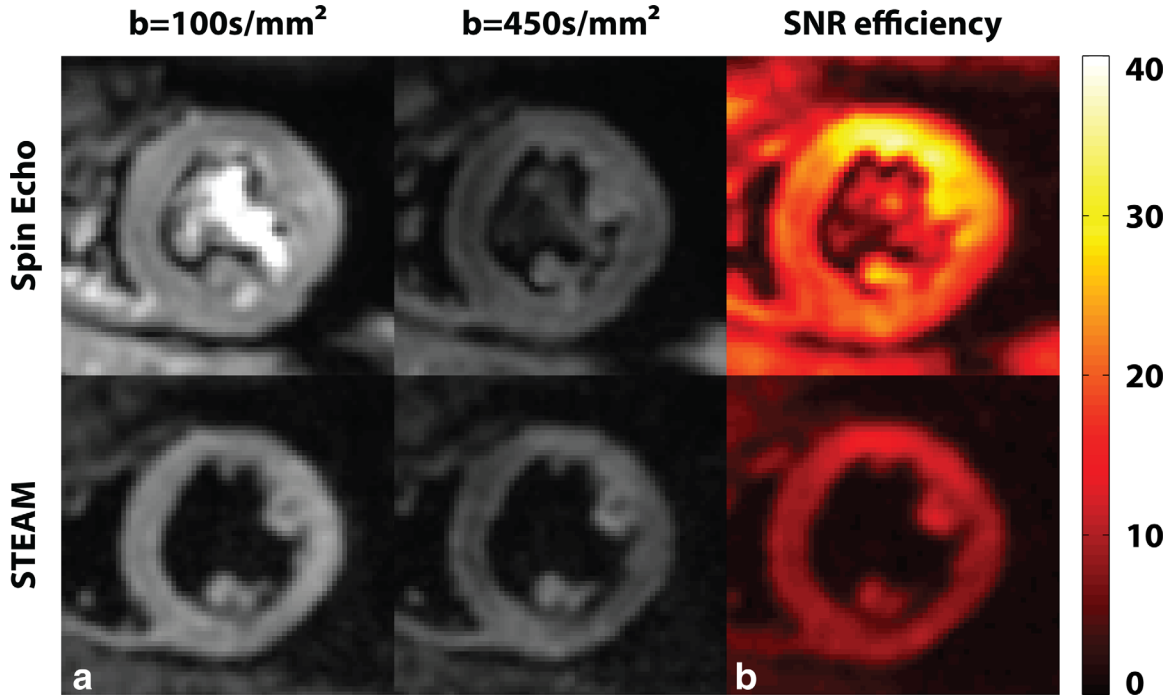STEAM

a   b

FIG. 3. In vivo data. **a:** Example dataset acquired at b = 100 s/mm² and 450 s/mm². **b:** Corresponding SNR efficiency maps for b = 450 s/mm².

$$B = \begin{bmatrix} b_{100} \begin{pmatrix} x^2_{diff01} & y^2_{diff01} & z^2_{diff01} & 2xy_{diff01} & 2xz_{diff01} & 2yz_{diff01} \\ & & \vdots & & & \\ x^2_{diff03} & y^2_{diff03} & z^2_{diff03} & 2xy_{diff03} & 2xz_{diff03} & 2yz_{diff03} \end{pmatrix} \begin{pmatrix} -1 \\ -1 \\ -1 \end{pmatrix} \\ b_{450} \begin{pmatrix} x^2_{diff04} & y^2_{diff04} & z^2_{diff04} & 2xy_{diff04} & 2xz_{diff04} & 2yz_{diff04} \\ & & \vdots & & & \\ x^2_{diff12} & y^2_{diff12} & z^2_{diff12} & 2xy_{diff12} & 2xz_{diff12} & 2yz_{diff12} \end{pmatrix} \begin{pmatrix} -1 \\ \vdots \\ -1 \end{pmatrix} \end{bmatrix}$$

[5]

b_{100} and b_{450} are the two heart rate adjusted b-values (nominal values: 100 and 450 s/mm²). $\vec{S}$ denotes the negative logarithmic signal vector

$$\vec{S} = -\ln([S_{\text{diff}01} \cdots S_{\text{diff}12}]^{\text{T}})$$ [6]

The $\vec{D}$ vector contains the diffusion tensor elements and the b = 0 s/mm² signal S_0:

$$\vec{D} = [D_{x^2} \ D_{y^2} \ D_{z^2} \ D_{xy} \ D_{xz} \ D_{yz} \ \ln(S_0)]^T$$ [7]

[†], T denote the Moore-Penrose pseudo inverse and transpose, respectively.

Upon tensor calculation the helix and transverse angles were calculated. Here the helix angle captures the local helix elevation, i.e., the angle between the projection of the first eigenvector of the diffusion tensor onto the epicardial surface and the transmural plane. The transverse angle represents the deviation of the helix from circumferential structure, i.e., the angle between the first eigenvector projected onto the radial circumferential plane and the circumferential contour (58). For each diffusion tensor, a normalized transmural position was calculated. Angle analysis was performed for the anterior, septal, inferior and lateral region separately. Furthermore, the gradient of a linear fit to the transmural helix angle course was calculated. Reproducibility of MD and FA were assessed by a two-tailed paired t-test and the Bland-Altman method (59).

RESULTS

SNR Measurements

Figure 3a shows example in vivo images for the b = 100 and 450 s/mm² acquisitions obtained by the SE and STEAM approach. The bright blood pool signal in the b = 100 s/mm² image of the SE measurements is dephased with increasing diffusion weighting. No signal contributions
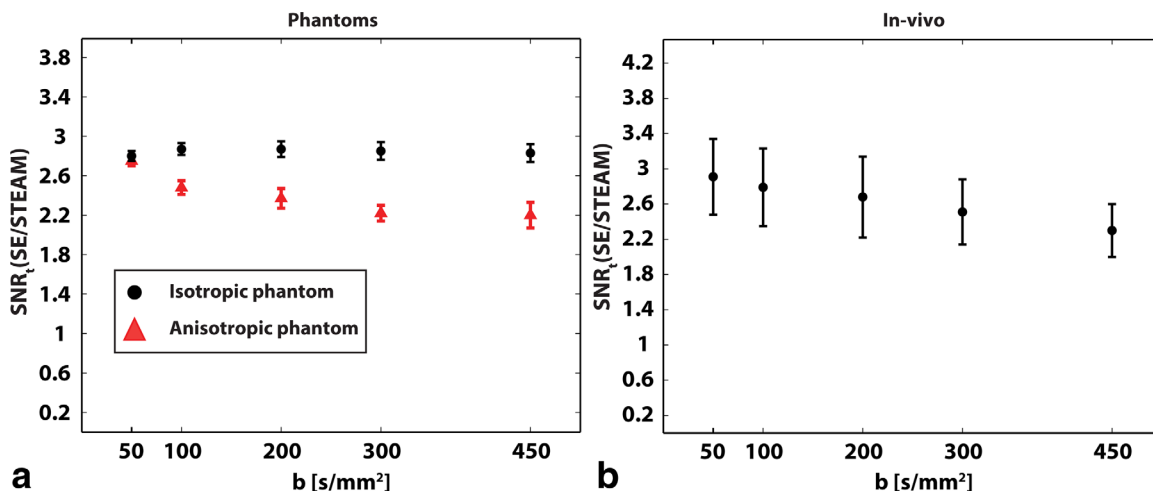
FIG. 4. SNR efficiency ratios of isotropic agar and anisotropic diffusion phantom as well as of in vivo measurements are shown for b-values ranging from 50 to 450 s/mm². **a:** While the isotropic agar phantom shows no b-value dependency, $SNR_t(SE/STEAM)$ is seen to decrease with increasing diffusion weighting in the anisotropic diffusion phantom. **b:** In vivo data reveal b-value dependency of $SNR_t(SE/STEAM)$ similar to anisotropic diffusion phantom.

from blood in the STEAM case are noticeable. SNR efficiency maps of SE and STEAM for a single average obtained with a b-value of 450 s/mm² are compared in Figure 3b.

SNR efficiency ratios $SNR_t(SE/STEAM)$ per single average of the phantom and in vivo data are plotted in Figure 4. The data of the isotropic agar phantom yielded a mean ratio of 2.84 ± 0.08, which agrees well with theory (theoretical $SNR_t(SE/STEAM) = 3.07$) as shown in Figure 4a. While $SNR_t(SE/STEAM)$ was independent of the b-value in the isotropic phantom, a distinct decrease of $SNR_t(SE/STEAM)$ was measured in the anisotropic diffusion phantom. Here the ratio of SNR efficiency for SE versus STEAM was found to decrease from 2.75 ± 0.05 to 2.20 ± 0.13 when increasing the b-value from 50 to 450 s/mm². The mean SNR efficiencies for the phantom measurements are listed in Supporting Tables S1 and S2. Similarly, the in vivo data revealed a reduced $SNR_t(SE/STEAM)$ with increasing b-value as shown in Figure 4b. The in vivo SNR efficiency ratios decreased from 2.91 ± 0.43 to 2.30 ± 0.30 when increasing the b-value from 50 s/mm² to 450 s/mm² (theoretical $SNR_t(SE/STEAM) = 3.46 ± 0.45$). The mean SNR efficiencies across all volunteers and b-values are listed in Supporting Table S3.

DTI Measurements

MD values obtained from SE data in the anisotropic diffusion phantom were found to be higher (1.58 ± 0.10 10^{-3}mm²/s) when compared with STEAM ($MD_{STEAM} = 1.14 ± 0.13$ 10^{-3}mm²/s). Likewise FA values obtained with SE were lower ($FA_{SE} = 0.29 ± 0.07$) relative to STEAM ($FA_{STEAM} = 0.53 ± 0.11$).

In vivo DTI data quality was assessed by calculating the percentage of negative eigenvalues. While 0.02 ± 0.05% of the diffusion tensors derived from SE were found to have negative eigenvalues, STEAM resulted in 2.53 ± 1.63%.

In Figure 5, example helix and transverse angle maps are compared for SE and STEAM. A clear progression in

helix angle from positive to negative values from endo- to epicardium can be observed. Reduced SNR in the STEAM case, however, causes patches with increased angle variations.

Statistics on helix and transverse angles across all volunteers for the anterior, septal, inferior and lateral segments are reported in Figure 6. The solid boxes and error bars correspond to the 50% and 90% percentiles of the helix angle distribution along the circumferential dimension. The linear dependency of the helix angles as a function of transmural depth is clearly evident for SE and STEAM. In the STEAM case, however, endo- and epicardial helix angles are found to be less steep with increased angle variation at the inferior–lateral region relative to SE. The root mean squared error (RMSE) of linear regression of the transmural helix angle distribution was found to be significantly reduced in SE versus STEAM (13.7 ± 2.6° versus 18.0 ± 2.8°; $P < 0.01$). The standard deviation of the transverse angles across all subjects and sectors was significantly smaller for SE compared with STEAM: (13.7 ± 1.2° versus 19.7 ± 2.0°; $P < 0.01$).

The reproducibility of MD and FA was determined by repeated acquisitions during one session. The average MD values were 1.43 ± 0.06 10^{-3}mm²/s for SE and 1.05 ± 0.08 10^{-3}mm²/s for STEAM. No statistically significant differences were found between repeated experiments for both SE and STEAM (SE: $P = 0.31$, STEAM: $P = 0.10$). However, differences for MD between SE and STEAM were statistically significant ($P < 0.001$). Mean FA values over all volunteers were 0.38 ± 0.02 for SE and 0.59 ± 0.03 for STEAM with no statistically significant differences between repeated experiments (SE: $P = 0.91$, STEAM: $P = 0.41$) in each case. However, FA differences between the SE and STEAM were statistically significant ($P < 0.001$). Corresponding Bland-Altman and line plots for the in vivo MD and FA values are shown in Figure 7.

Figure 8 shows the distribution of the first, second and third eigenvectors (e1, e2, e3) for SE and STEAM DTI
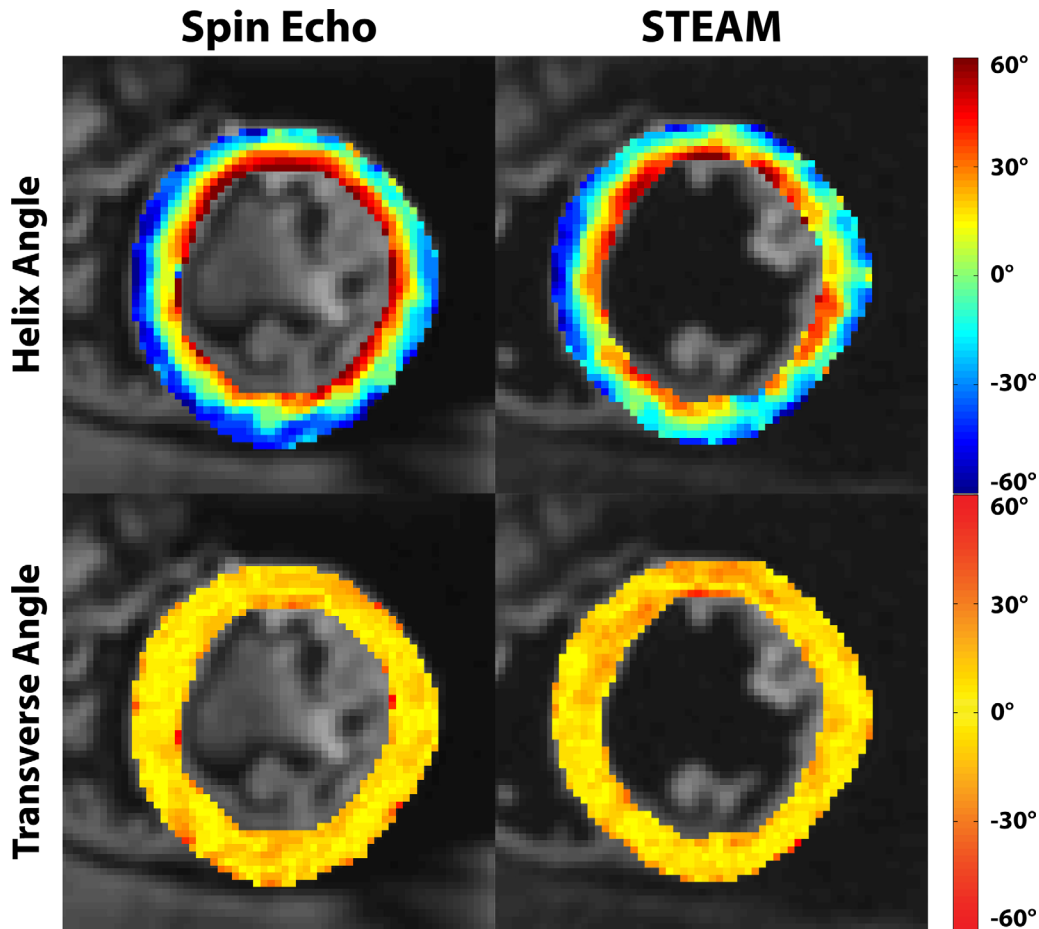
FIG. 5. Helix and transverse angle maps. The linear decrease of helix angles from endo- to epicardium is visible, however more coherent in the SE case. Transverse angles are close to zero degrees for both sequences except for nonnegative values at the intersection of left and right ventricular structures and near the papillary muscles.
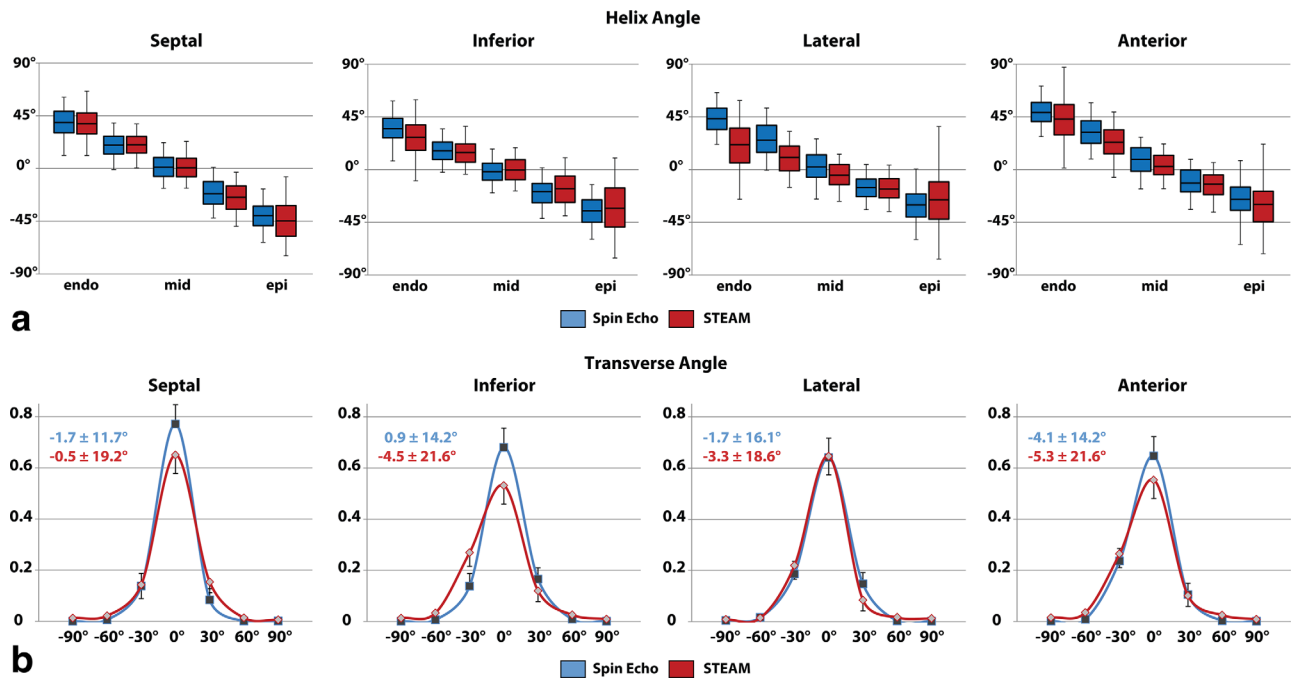
FIG. 6. Sectorwise helix and transverse angle statistics. **a:** Comparison of transmural helix angle distribution for SE (blue) and STEAM (red) (solid box: 50% percentile, error bars: 90% percentile of the helix angle distribution in circumferential direction). Helix angle variations are more pronounced in STEAM, particularly at the endo- and epicardial region. **b:** Histograms of transverse angles show reduced dispersion of transverse angle for SE.
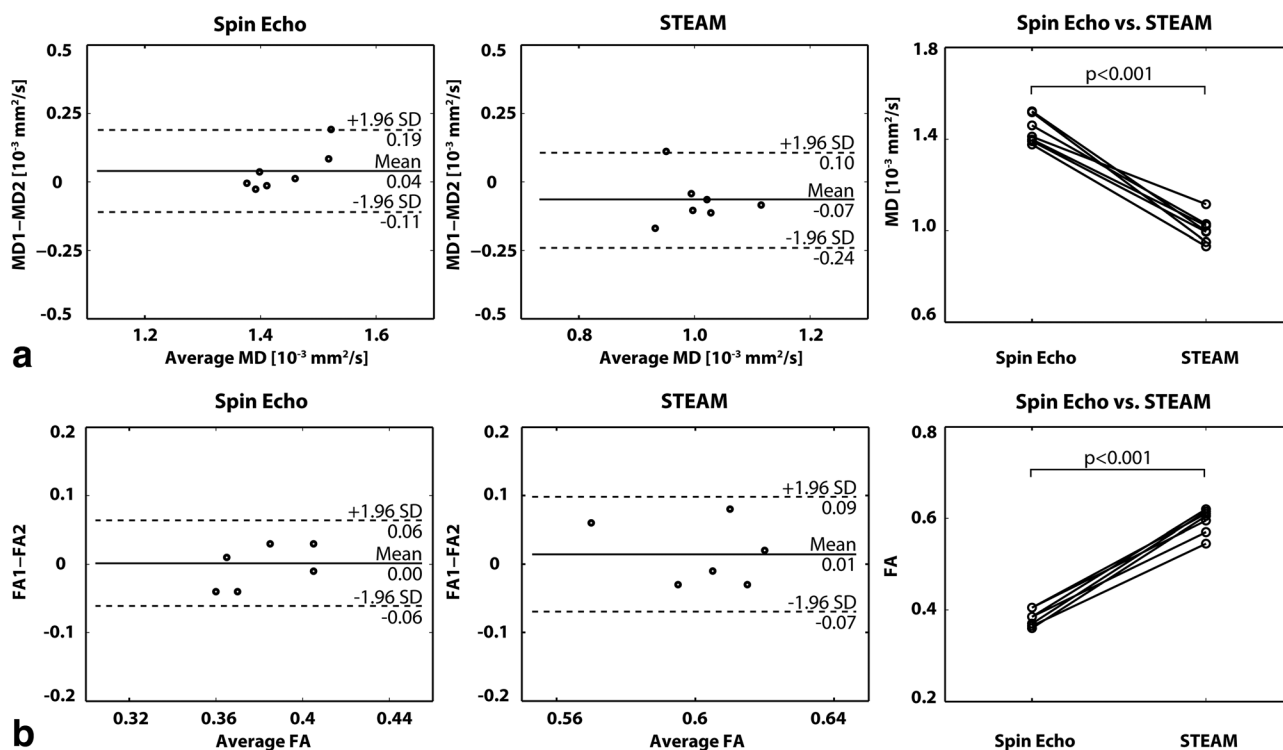
FIG. 7. Bland-Altman and line plots of MD (**a**) and FA (**b**) representing intra subject reproducibility of SE versus STEAM. No statistical differences were observed between repeat measurements for MD and FA for both SE and STEAM. Significant differences were found for MD and FA between both sequences.

data across all volunteers. The SE distributions show narrow, almost equally high distinct peaks, whereas the eigenvalue spectrum in the STEAM case is broadened. The small percentage of negative eigenvalues (e3) in the STEAM case can be appreciated as well. Furthermore, the maximums of the SE eigenvalue distributions are increased and less separate relative to STEAM, in agreement with the results for MD and FA.

DISCUSSION

In this study the relative SNR gain of cardiac-triggered, motion-compensated SE diffusion tensor imaging with respect to STEAM has been demonstrated using both phantom and in vivo data. The SNR gain was found to improve the accuracy of diffusion metrics including helix and transverse angle maps.

At a b-value of 50 s/mm^2 the measured SNR efficiency gain of 2.84 of SE versus STEAM agreed well with theory in the phantoms. In vivo, the measured gain in SNR efficiency at the lowest b-value was smaller compared with theory [2.91 ± 0.21 (in vivo) versus 3.46 ± 0.45 (theory)]. This is attributed in parts to slice profile imperfections of the VERSE echo pulse (56) and partial volume effects through-slice in vivo. All SNR measurements were obtained from a single signal average. Thereby confounding factors due to image misregistration and phase correction for averaging of complex data were avoided. To facilitate these measurements, the slice thickness was increased to 16 mm contributing to increased partial voluming.

While the ratio of SNR efficiency of SE versus STEAM was found to be independent of the b-value in the isotropic agar phantom, decreasing values were measured with increasing b-value for both the anisotropic diffusion phantom and in the in vivo myocardium. This result is explained by differences in diffusion times ΔT (ΔT_{STEAM} = 1000 ms versus ΔT_{SE} = 25 ms) (60,61). Assuming a mean diffusivity of 1.4 × 10^{-3}mm^2/s and diffusion times of 25 ms for SE and 1000 ms for STEAM, the diffusion length is approximately 15 and 90 μm, respectively. In comparison, the thickness of cardiac myocytes is in the range of approximately 10–20 μm (62,63). Hence, diffusion becomes restricted during STEAM encoding and diffusion induced phase distributions deviate from a Gaussian shape (64). The phase distribution in STEAM is expected to be stretched out along the fiber direction due to the long diffusion time and the lateral confinement by myofibers.

DTI data were acquired with a modified sampling method. Instead of acquiring a b = 0 s/mm^2 image, three directions with a b-value of 100 s/mm^2 and nine directions with a b-value of 450 s/mm^2 were sampled. Thereby the effect of in vivo perfusion was reduced (65–67). Helix angle maps obtained with SE and STEAM revealed the expected linear decrease from endo- to epicardium in accordance with previous studies (13,16,18,21,23). However, STEAM data resulted in increased deviation from the linear function when compared with SE, in particular in the inferior–lateral region, which corresponds to areas of low SNR in the SNR efficiency maps. The drop in SNR is related to the distal
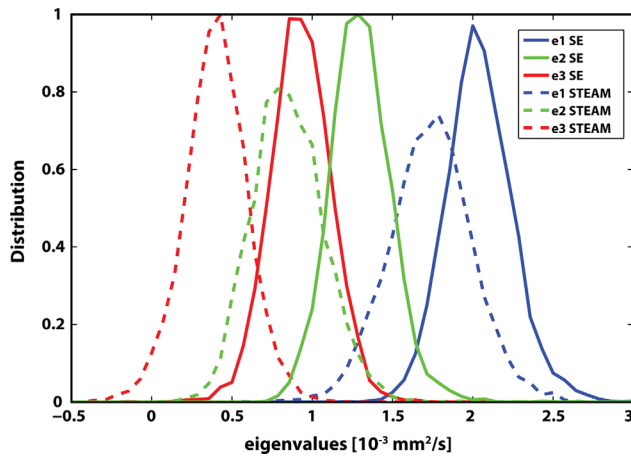
FIG. 8. Eigenvalue analysis. Diffusion tensor eigenvalue (e1, e2, e3) histograms for SE (solid line) and STEAM (dashed line). SE eigenvalues show a distinct and dense distribution, while STEAM eigenvalue histograms are broadened.

positon of the inferior–lateral segment to the surface coils.

In this region of low SNR, the helix angle range was found to be underestimated compared with SE. Transverse angles were measured close to zero degrees on average, describing the circumferential alignment of myofibers. The lower SNR of STEAM, however, caused a larger variation around zero when compared with SE.

In vivo results for MD and FA were reproducible and in accordance with literature values of the in vivo human heart (13,16,18,21,23,38). Significant differences in MD and FA were seen between in vivo STEAM and SE similar to previous results found in muscle tissue (60). The measurements in the anisotropic diffusion phantom confirmed these findings. While MD is higher in the SE case, FA is increased with STEAM. Increased fractional anisotropy FA_{STEAM} is represented by a broad separation of the eigenvalue distributions compared with a compact, distinct distribution pattern in the SE case.

By design, the total scan duration for breath-held SE and STEAM imaging was kept identical in this study. However, SE acquisitions are favored for time-efficient free-breathing acquisitions as demonstrated in the supplemental material. In contrast, free-breathing STEAM imaging requires a very narrow respiratory gating window between the second (decoding) and first (encoding) heartbeat (18) hence reducing scan efficiency significantly relative to SE. As demonstrated in the supplemental material, SE resulted in 30% increased scan efficiency compared with STEAM while SNR and DTI results were in very good agreement with the findings from the breath-hold measurements.

Acceleration compensated spin-echo cardiac DTI requires a high-performance gradient system to reduce TE to approximately 65–70 ms for a b-value of 450 s/mm^2. With the recent introduction of clinical MR machines with high-performance gradient systems, this requirement is expected to be met increasingly in the near future.

CONCLUSIONS

Cardiac diffusion tensor imaging using motion-compensated SE yields up to 2.9× increase in SNR efficiency relative to STEAM, which in turn translates to reduced deviation of helix and transverse angles from expected in vivo configurations. The SE method hence presents an attractive alternative to STEAM based approaches for cardiac diffusion tensor imaging of the in vivo heart on modern MR systems with high-performance gradients.

APPENDIX

Because the SE approach requires only one cardiac cycle to acquire a diffusion weighted image (in contrast to two R–R intervals for STEAM), the sequence is particularly suited for free-breathing navigator gated acquisition.

DTI acquisition was performed during free-breathing with a navigator gating scheme as proposed by Nielles-Vallespin et al (18) along three (b = 100 s/mm^2) and nine (b = 450 s/mm^2) diffusion directions without visual feedback system. Images were accepted if the first navigator of the STEAM sequence was within the acceptance window of 5 mm and the second navigator had a relative displacement of less than ±0.5 mm to the first one. The imaging parameters were identical to the parameters used for breath-held imaging: resolution 2.8 × 2.8 mm^2, slice thickness 8 mm, FOV: 230 × 98 mm^2, TE/TR(SE): 70 ms/1-R-R, TE/TR(STEAM): 31 ms/2-R-R, signal averages SE/STEAM: 16/8. Imaging was timed to the systolic strain "sweet spot" (15). DTI analysis was performed based on mean diffusivity (MD), fractional anisotropy (FA), helix and transverse angles, the percentage of negative eigenvalues of the diffusion tensor and scan time efficiency. SNR was measured in a separate scan for b = 50 and 450 s/mm^2 along six diffusion directions (16 mm slice thickness), four signal averages. DTI data reproducibility was not part of this sub-study.

SE based DTI data acquisition was 30% faster than STEAM for all volunteers (7:06 ± 3:09 min:s versus 9:52 ± 2:25 min:s). Supplementary Figure S1a shows an example helix and transverse angle map. Similar to the breath-hold acquisition (Fig. 5), the helix map for STEAM shows patches with increased angle variations and less steep angles endo- and epicardially. A linear transmural change of helix angles can be seen in Supplementary Figure S1b. Transverse angles were close to zero degrees with wider spread in the STEAM (-1.2 ± 18.7)° case compared with SE (-2.2 ± 14.5)°. The RMSE of linear regression of the transmural helix angle distribution was reduced in all cases for SE versus STEAM (14.0 ± 0.7° versus 17.1 ± 1.5°). While 3.7 ± 1.7% of the diffusion tensors derived from STEAM had negative eigenvalues, no negative eigenvalue was found in the SE case. The average MD values were 1.48 ± 0.11 10^{-3}mm^2/s for SE and 0.99 ± 0.06 10^{-3}mm^2/s for STEAM. Mean FA values over all volunteers were 0.37 ± 0.04 for SE and 0.61 ± 0.03 for STEAM. MD and FA were in accordance with breath-hold and literature values (13,16,18,21,23,38).

Similar to the breath-hold measurements, the in vivo data show a $SNR_t(SE/STEAM)$ of 3.12 ± 0.66 to 2.79 ± 0.51 with increasing b-value from 50 s/mm^2 to 450 s/mm^2 (theoretical $SNR_t(SE/STEAM) = 3.73 \pm 0.67$).

In summary, free-breathing DTI and SNR results are in very good agreement with the results from breath-hold acquisitions of this work and similar to previous studies (18,23). In addition, scan time efficiency was significantly improved for SE compared with STEAM. Hence, besides the SNR benefit, free-breathing navigator gating efficiency is increased when using SE based DTI.

REFERENCES

1. Smerup M, Partridge J, Agger P, Ringgaard S, Pedersen M, Petersen S, Hasenkam JM, Niederer P, Lunkenheimer PP, Anderson RH. A mathematical model of the mechanical link between shortening of the cardiomyocytes and systolic deformation of the left ventricular myocardium. Technol Health Care 2013;21:63–79.

2. Sano T, Takayama N, Shimamoto T. Directional difference of conduction velocity in the cardiac ventricular syncytium studied by microelectrodes. Circ Res 1959;7:262–267.

3. Vadakkumpadan F, Arevalo H, Ceritoglu C, Miller M, Trayanova N. Image-based estimation of ventricular fiber orientations for personalized modeling of cardiac electrophysiology. IEEE Trans Med Imaging 2012;31:1051–1060.

4. Lee LC, Genet M, Dang AB, Ge L, Guccione JM, Ratcliffe MB. Applications of computational modeling in cardiac surgery. J Card Surg 2014;29:293–302.

5. Genet M, Lee LC, Nguyen R, Haraldsson H, Acevedo-Bolton G, Zhang Z, Ge L, Ordovas K, Kozerke S, Guccione JM. Distribution of normal human left ventricular myofiber stress at end diastole and end systole: a target for in silico design of heart failure treatments. J Appl Physiol 2014;117:142–152.

6. Pope AJ, Sands GB, Smaill BH, LeGrice IJ. Three-dimensional transmural organization of perimysial collagen in the heart. Am J Physiol Heart Circ Physiol 2008;295:H1243–H1252.

7. Young AA, Legrice IJ, Young MA, Smaill BH. Extended confocal microscopy of myocardial laminae and collagen network. J Microsc 1998;192:139–150.

8. Costa KD, Takayama Y, McCulloch AD, Covell JW. Laminar fiber architecture and three-dimensional systolic mechanics in canine ventricular myocardium. Am J Physiol 1999;276:H595–H607.

9. Geerts L, Bovendeerd P, Nicolay K, Arts T. Characterization of the normal cardiac myofiber field in goat measured with MR-diffusion tensor imaging. Am J Physiol Heart Circ Physiol 2002;283:H139–45.

10. Helm PA, Tseng HJ, Younes L, McVeigh ER, Winslow RL. Ex vivo 3D diffusion tensor imaging and quantification of cardiac laminar structure. Magn Reson Med 2005;54:850–859.

11. Lombaert H, Peyrat JM, Croisille P, Rapacchi S, Fanton L, Cheriet F, Clarysse P, Magnin I, Delingette H, Ayache N. Human atlas of the cardiac fiber architecture: study on a healthy population. IEEE Trans Med Imaging 2012;31:1436–1447.

12. Edelman RR, Gaa J, Wedeen VJ, Loh E, Hare JM, Prasad P, Li W. In vivo measurement of water diffusion in the human heart. Magn Reson Med 1994;32:423–428.

13. Dou J, Reese TG, Tseng WY, Wedeen VJ. Cardiac diffusion MRI without motion effects. Magn Reson Med 2002;48:105–114.

14. Tseng WY, Reese TG, Weisskoff RM, Brady TJ, Wedeen VJ. Myocardial fiber shortening in humans: initial results of MR imaging. Radiology 2000;216:128–139.

15. Tseng WI, Reese TG, Weisskoff RM, Wedeen VJ. Cardiac diffusion tensor MRI in vivo without strain correction. Magn Reson Med 1999;42:393–403.

16. Gamper U, Boesiger P, Kozerke S. Diffusion imaging of the in vivo heart using spin echoes--considerations on bulk motion sensitivity. Magn Reson Med 2007;57:331–337.

17. Toussaint N, Sermesant M, Stoeck CT, Kozerke S, Batchelor PG. In vivo human 3D cardiac fibre architecture: reconstruction using curvilinear interpolation of diffusion tensor images. Med Image Comput Comput Assist Interv 2010;13:418–425.

18. Nielles-Vallespin S, Mekkaoui C, Gatehouse P, Reese TG, Keegan J, Ferreira PF, Collins S, Speier P, Feiweier T, Silva R. In vivo diffusion tensor MRI of the human heart: Reproducibility of breath-hold and navigator-based approaches. Magn Reson Med 2013;70:454–465.

19. Toussaint N, Stoeck CT, Schaeffter T, Kozerke S, Sermesant M, Batchelor PG. In vivo human cardiac fibre architecture estimation using shape-based diffusion tensor processing. Med Image Anal 2013;17:1243–1255.

20. Reese TG, Wedeen VJ, Weisskoff RM. Measuring diffusion in the presence of material strain. J Magn Reson B 1996;112:253–258.

21. Reese TG, Weisskoff RM, Smith RN, Rosen BR, Dinsmore RE, Wedeen VJ. Imaging myocardial fiber architecture in vivo with magnetic resonance. Magn Reson Med 1995;34:786–791.

22. Wu MT, Tseng WY, Su MY, Liu CP, Chiou KR, Wedeen VJ, Reese TG, Yang CF. Diffusion tensor magnetic resonance imaging mapping the fiber architecture remodeling in human myocardium after infarction: correlation with viability and wall motion. Circulation 2006;114:1036–1045.

23. Stoeck CT, Kalinowska A, von Deuster C, et al. Dual-phase cardiac diffusion tensor imaging with strain correction. PLoS One 2014;9:e107159.

24. Wei H, Viallon M, Delattre B, Moulin K, Yang F, Croisille P, Zhu Y. Free-breathing diffusion tensor imaging and tractography of the human heart in healthy volunteers using wavelet-based image fusion. IEEE Trans Med Imaging 2015;34:306–316.

25. Streeter DD Jr, Spotnitz HM, Patel DP, Ross J Jr, Sonnenblick EH. Fiber orientation in the canine left ventricle during diastole and systole. Circ Res 1969;24:339–347.

26. Greenbaum RA, Ho SY, Gibson DG, Becker AE, Anderson RH. Left ventricular fibre architecture in man. Br Heart J 1981;45:248–263.

27. Schmid P, Jaermann T, Boesiger P, Niederer PF, Lunkenheimer PP, Cryer CW, Anderson RH. Ventricular myocardial architecture as visualised in postmortem swine hearts using magnetic resonance diffusion tensor imaging. Eur J Cardiothoracic Surg 2005;27:468–472.

28. Chen J, Song SK, Liu W, McLean M, Allen JS, Tan J, Wickline SA, Yu X. Remodeling of cardiac fiber structure after infarction in rats quantified with diffusion tensor MRI. Am J Physiol Heart Circ Physiol 2003;285:H946–H954.

29. Sosnovik DE, Wang R, Dai G, Wang T, Aikawa E, Novikov M, Rosenzweig A, Gilbert RJ, Wedeen VJ. Diffusion spectrum MRI tractography reveals the presence of a complex network of residual myofibers in infarcted myocardium. Circ Cardiovasc Imaging 2009;2:206–212.

30. Wu EX, Wu Y, Nicholls JM, Wang J, Liao S, Zhu S, Lau CP, Tse HF. MR diffusion tensor imaging study of postinfarct myocardium structural remodeling in a porcine model. Magn Reson Med 2007;58:687–695.

31. Strijkers GJ, Bouts A, Blankesteijn WM, Peeters TH, Vilanova A, van Prooijen MC, Sanders HM, Heijman E, Nicolay K. Diffusion tensor imaging of left ventricular remodeling in response to myocardial infarction in the mouse. NMR Biomed 2009;22:182–190.

32. Mekkaoui C, Huang S, Chen HH, Dai G, Reese TG, Kostis WJ, Thiagalingam A, Maurovich-Horvat P, Ruskin JN, Hoffmann U. Fiber architecture in remodeled myocardium revealed with a quantitative diffusion CMR tractography framework and histological validation. J Cardiovasc Magn Reson 2012;14:70.

33. Tseng WY, Dou J, Reese TG, Wedeen VJ. Imaging myocardial fiber disarray and intramural strain hypokinesis in hypertrophic cardiomyopathy with MRI. J Magn Reson Imaging 2006;23:1–8.

34. Wu MT, Su MY, Huang YL, Chiou KR, Yang P, Pan HB, Reese TG, Wedeen VJ, Tseng WY. Sequential changes of myocardial microstructure in patients postmyocardial infarction by diffusion-tensor cardiac MR: correlation with left ventricular structure and function. Circ Cardiovasc Imaging 2009;2:32–40, 6 p following 40.

35. Wei H, Viallon M, Delattre BM, Wang L, Pai VM, Wen H, Xue H, Guetter C, Croisille P, Zhu Y. Assessment of cardiac motion effects on the fiber architecture of the human heart in vivo. IEEE Trans Med Imaging 2013;32:1928–1938.

36. Froeling M, Strijkers G, Nederveen AJ, Chamuleau SA, Luijten PR. Diffusion tensor MRI of the heart – in vivo imaging of myocardial fiber architecture. Curr Cardiovasc Imaging Rep 2014;7:1–11.

37. Sosnovik DE, Mekkaoui C, Huang S, et al. Microstructural impact of ischemia and bone marrow-derived cell therapy revealed with diffusion tensor magnetic resonance imaging tractography of the heart in vivo. Circulation 2014;129:1731–1741.

38. Stoeck CT, von Deuster C, Genet M, Atkinson D, Kozerke S. Second order motion compensated spin-echo diffusion tensor imaging of the human heart. Magn Reson Med 2016;75:1669–1676.

39. Nguyen C, Fan Z, Sharif B, He Y, Dharmakumar R, Berman DS, Li D. In vivo three-dimensional high resolution cardiac diffusion-weighted MRI: A motion compensated diffusion-prepared balanced steady-state free precession approach. Magn Reson Med 2014;72:1257–1267.

40. Stoeck CT, von Deuster C, Toussaint N, Kozerke S. High-resolution single-shot DTI of the in-vivo human heart using asymmetric diffusion encoding. In Proceedings of the 21st Annual Meeting of ISMRM, Salt Lake City, Utah, USA, 2013. Abstract 480.

41. Stoeck CT, Toussaint N, Boesiger P, Batchelor PG, Kozerke S. Sequence timing optimization in multi-slice diffusion tensor imaging of the beating heart. In Proceedings of the 19th Annual Meeting of ISMRM, Montréal, Canada, 2011. Abstract 282.

42. Welsh C, Di Bella E, Hsu E. Higher-order motion-compensation for in vivo cardiac diffusion tensor imaging in rats. IEEE Trans Med Imaging 2015;34:1843–1853.

43. Nakamura T, Shibukawa S, Muro I, Kajihara N, Nishio H, Ogini T, Niwa T, Imai Y. Improvement of visualization of cardiac wall in diffusion-weighted imaging using cardiac triggering and acceleration motion correction. In Proceedings of the 22nd Annual Meeting of ISMRM, Milan, Italy, 2014. Abstract 2417.

44. Chan RW, von Deuster C, Giese D, Stoeck CT, Harmer J, Aitken AP, Atkinson D, Kozerke S. Characterization and correction of eddy-current artifacts in unipolar and bipolar diffusion sequences using magnetic field monitoring. J Magn Reson 2014;244:74–84.

45. Pai VM, Rapacchi S, Kellman P, Croisille P, Wen H. PCATMIP: enhancing signal intensity in diffusion-weighted magnetic resonance imaging. Magn Reson Med 2011;65:1611–1619.

46. McGill LA, Ismail TF, Nielles-Vallespin S, et al. Reproducibility of in-vivo diffusion tensor cardiovascular magnetic resonance in hypertrophic cardiomyopathy. J Cardiovasc Magn Reson 2012;14:86.

47. Ferreira P, Kilner PJ, McGill L-A, et al. In vivo cardiovascular magnetic resonance diffusion tensor imaging shows evidence of abnormal myocardial laminar orientations and mobility in hypertrophic cardiomyopathy. J Cardiovasc Magn Reson 2014;16:P338.

48. Nguyen C, Fan Z, Xie Y, Dawkins J, Tseliou E, Bi X, Sharif B, Dharmakumar R, Marbán E, Li D. In vivo contrast free chronic myocardial infarction characterization using diffusion-weighted cardiovascular magnetic resonance. J Cardiovasc Magn Reson 2014;16:1–10.

49. Montant P, Sigovan M, Revel D, Douek P. MR imaging assessment of myocardial edema with T2 mapping. Diagn Interv Imaging 2015;96:885–890.

50. Germain P, El Ghannudi S, Jeung MY, Ohlmann P, Epailly E, Roy C, Gangi A. Native T1 mapping of the heart - a pictorial review. Clin Med Insights Cardiol 2014;8:1–11.

51. Cuppen JJM. RLSQ: T1, T2, and ρ calculations, combining ratios and least squares. Magn Reson Med 1987;5:513–524.

52. Reischauer C, Staempfli P, Jaermann T, Boesiger P. Construction of a temperature-controlled diffusion phantom for quality control of diffusion measurements. J Magn Reson Imaging 2009;29:692–698.

53. Froeling M, Nederveen AJ, Nicolay K, Strijkers GJ. DTI of human skeletal muscle: the effects of diffusion encoding parameters, signal-to-noise ratio and T2 on tensor indices and fiber tracts. NMR Biomed 2013;26:1339–1352.

54. Feinberg DA, Setsompop K. Ultra-fast MRI of the human brain with simultaneous multi-slice imaging. J Magn Reson 2013;229:90–100.

55. Meyer CH, Pauly JM, Macovski A, Nishimura DG. Simultaneous spatial and spectral selective excitation. Magn Reson Med 1990;15:287–304.

56. Hargreaves BA, Cunningham CH, Nishimura DG, Conolly SM. Variable-rate selective excitation for rapid MRI sequences. Magn Reson Med 2004; 52:590–597.

57. Klein S, Staring M, Murphy K, Viergever MA, Pluim JP. elastix: a toolbox for intensity-based medical image registration. IEEE Trans Med Imaging 2010;29:196–205.

58. Scollan DF, Holmes A, Winslow R, Forder J. Histological validation of myocardial microstructure obtained from diffusion tensor magnetic resonance imaging. Am J Physiol 1998;275:H2308–H2318.

59. Bland JM, Altman DG. Statistical methods for assessing agreement between two methods of clinical measurement. Lancet 1986;1:307–310.

60. Noehren B, Andersen A, Feiweier T, Damon B, Hardy P. Comparison of twice refocused spin echo versus stimulated echo diffusion tensor imaging for tracking muscle fibers. J Magn Reson Imaging 2015;41:624–632.

61. Froeling M, Mazzoli V. Ex vivo cardiac DTI: on the effects of diffusion time and b-value. J Cardiovasc Magn Reson 2011;16:P77.

62. Spotnitz HM, Spotnitz WD, Cottrell TS, Spiro D, Sonnenblick EH. Cellular basis for volume related wall thickness changes in the rat left ventricle. J Mol Cell Cardiol 1974;6:317–331.

63. Gerdes AM, Moore JA, Hines JM, Kirkland PA, Bishop SP. Regional differences in myocyte size in normal rat heart. Anat Rec 1986;215:420–426.

64. Mazzoli V, Froeling M, Nederveen AJ, Nicolay K, Strijkers GJ. Cardiac diffusion MRI beyond DTI. In Proceedings of the 22nd Annual Meeting of ISMRM, Milan, Italy, 2014. Abstract 2560.

65. Scott AD, Ferreira PF, Nielles-Vallespin S, Gatehouse P, McGill L-A, Kilner P, Pennell DJ, Firmin DN. Optimal diffusion weighting for in vivo cardiac diffusion tensor imaging. Magn Reson Med 2015;74:420–430.

66. Le Bihan D, Breton E, Lallemand D, Aubin ML, Vignaud J, Laval-Jeantet M. Separation of diffusion and perfusion in intravoxel incoherent motion MR imaging. Radiology 1988;168:497–505.

67. Callot V, Bennett E, Decking UKM, Balaban RS, Wen H. In vivo study of microcirculation in canine myocardium using the IVIM method. Magn Reson Med 2003;50:531–540.

SUPPORTING INFORMATION

Additional Supporting Information may be found in the online version of this article.

Supporting Table S1. Results of SNR efficiency of SE versus STEAM measured in isotropic agar phantom for different b-values.
Supporting Table S2. Results of SNR efficiency measured in anisotropic diffusion phantom.
Supporting Table S3. Results of SNR efficiency of SE versus STEAM measured in vivo for different b-values.
Supporting Figure S1. Free breathing acquisition: a) Helix and transverse angle maps. Similar to the breath hold case, the decrease of helix angles from endo- to epicardium is more coherent for SE. Transverse angles are close to zero degrees. b) Helix and transverse angle statistics: Comparison of transmural helix angle distribution for SE (blue) and STEAM (red) (solid box: 50% percentile, error bars: 90% percentile of the helix angle distribution in circumferential direction).